

# Record-Low-Threshold Lasers Based on Atomically Smooth Triangular Nanoplatelet Perovskite

Guohui Li, Tao Che, Xingqi Ji, Shaoding Liu, Yuying Hao, Yanxia Cui,\*  
and Shengzhong Liu\*

Single-crystalline perovskites are ideal candidates for lasing and other optoelectronic applications. Although significant efforts have been made to grow both bulk single-crystalline perovskites in liquid solution, their dimensions are still too large to make nanoscale whispering-gallery-mode (WGM) resonator based lasers that possess high quality (Q) factor and small volume. Besides, most reported perovskite resonators do not possess atomically smooth surfaces and facets, which limits the Q and thereby increases the lasing threshold. Here, atomically smooth triangular  $\text{PbI}_2$  templates are fabricated on a mica substrate by the vapor phase deposition method and are converted to atomically smooth perovskites which have regular and unwrinkled facets with average surface roughness less than 2 nm. By using a  $\text{CH}_3\text{NH}_3\text{PbI}_3$  nanoplatelet with a side length of 27  $\mu\text{m}$  and thickness of 80 nm, room temperature WGM lasing with a Q up to 2600 is demonstrated, the highest reported for hybrid organic–inorganic perovskite nanoplatelets. In addition, the volume of the WGM mode is reduced significantly in comparison with the prior reports. The realized high-quality triangular  $\text{CH}_3\text{NH}_3\text{PbI}_3$  perovskite nanoplatelets with high Q factor and small volume are expected to perform as ideal cavities for long pulse durations lasers and would find potential applications in integrated optoelectronic devices.

## 1. Introduction

Compared with traditional semiconductor materials, perovskite, as a rising star semiconductor material,<sup>[1,2]</sup> has shown great potential in optoelectronic applications including photovoltaics, lasers, photodetectors, and light emitting diodes,<sup>[3–6]</sup> attributed to its advantages such as long carrier lifetimes ( $10^{1-2}$  ns), long diffusion length, high fluorescence yield, wavelength tunability, etc.<sup>[7,8]</sup> Although great efforts have been made to develop high-performance polycrystalline or microcrystalline perovskite films, the single-crystalline perovskite samples are more promising for realizing high-performance optoelectronic devices due to their reduced amounts of grain boundaries and the corresponding extremely low trap densities.<sup>[9–11]</sup> To fabricate high-quality perovskite bulk single crystals, the liquid growth method with different strategies to reduce the solubility of the target sample in a precursor solution was adopted.<sup>[12–15]</sup> Beyond the bulk perovskite


crystals, geometry-controllable perovskite crystals in the forms of thin-plate, column-shaped, and pillar arrays have also been developed by confining the crystal growth within specific spaces through the use of templates.<sup>[16]</sup> However, the template-assisted perovskite crystals usually have dimensions on the microscale, and their growth in the liquid environment cannot provide atomically smooth surfaces and facets, which are prerequisites for producing high-quality-factor lasers.

For laser applications, nanoscale semiconductor devices are highly attractive owing to their ultracompact physical sizes, highly localized coherent outputs, efficient waveguiding, and high suitability to integration.<sup>[17–22]</sup> Whispering-gallery-mode (WGM) resonators have been demonstrated as excellent candidates for making semiconductor lasers because of their high quality (Q) factor and small volume (V),<sup>[23–28]</sup> and a large Q/V permits strong coupling between the gain medium and the cavity field, which enables the realization of low-threshold and narrow-linewidth lasers.<sup>[23]</sup> To obtain the nanoscale perovskite WGM resonators, either the vapor growth method or the self-assembly method are usually adopted.<sup>[1,29]</sup> Both hybrid organic–inorganic perovskite materials and inorganic perovskite WGM resonators have been widely studied

Dr. G. Li, T. Che, X. Ji, Prof. S. Liu, Prof. Y. Hao, Prof. Y. Cui  
Key Lab of Advanced Transducers and Intelligent Control  
System of Ministry of Education  
College of Physics and Optoelectronics  
Key Laboratory of Interface Science and Engineering  
in Advanced Materials  
Taiyuan University of Technology  
Taiyuan 030024, P. R. China  
E-mail: yanxiacui@gmail.com

Prof. Y. Cui  
State Key Laboratory of Quantum Optics and Quantum Optics Devices  
Shanxi University  
Taiyuan 030006, P. R. China

Prof. S. Liu  
Key Laboratory of Applied Surface and Colloid  
Chemistry National Ministry of Education  
Shaanxi Engineering Lab for Advanced Energy  
Technology School of Materials Science and Engineering  
Shaanxi Normal University  
Xi'an 710119, P. R. China  
E-mail: szliu@dicp.ac.cn

 The ORCID identification number(s) for the author(s) of this article can be found under <https://doi.org/10.1002/adfm.201805553>.

DOI: 10.1002/adfm.201805553

for various laser applications.<sup>[30–36]</sup> Methylammonium lead halide ( $\text{CH}_3\text{NH}_3\text{PbX}_3$ ) perovskites, as hybrid organic–inorganic semiconductors, have been demonstrated to be among the promising gain materials for nanolasers,<sup>[33–36]</sup> which have been intensely studied in various structures with different geometries, such as micro/nanoplatelets (or disks), nanowires, microspheres, microrods, and distributed bragg reflector mirrors for diverse application needs. Specifically, perovskite nanoplatelets (NPLs) realizing lasing through WGM modes are of particular interest in applications of spectroscopy and high-throughput biosensing.<sup>[2]</sup> In 2014, the original  $\text{CH}_3\text{NH}_3\text{PbI}_3$  NPL-based laser, produced through the vapor phase deposition method, was demonstrated by Zhang et al. and achieved a lasing threshold of  $37 \mu\text{J cm}^{-2}$  and a Q of 650.<sup>[1]</sup> Based on a one-step solution self-assembly method,  $\text{CH}_3\text{NH}_3\text{PbX}_3$  microdisks were also synthesized at the same time, but they displayed a relatively lower Q ( $\approx 430$ ) compared with those realized by the vapor deposition method.<sup>[2]</sup> Later, Liu et al. fabricated patterned  $\text{CH}_3\text{NH}_3\text{PbI}_3$  NPLs on silicon substrate with a buffer layer, yielding WGM lasing with a Q of 1210.<sup>[36]</sup> Perumal et al. fabricated hexagonal-like  $\text{CH}_3\text{NH}_3\text{PbI}_3$  grains based on a one-step solution self-assembly method, as well, and they realized WGM lasing with a threshold of  $26.8 \mu\text{J cm}^{-2}$  and a Q of 1200.<sup>[29]</sup> The lasing properties of these perovskite devices based on micro/NPLs (or disks) can also be freely tuned by utilizing rectangular microdisks connected by a straight waveguide,<sup>[37]</sup> hexagonal grains with  $\text{SiO}_2$  spheres,<sup>[29]</sup> and so on.

All the perovskite lasers reported to date were pumped optically. It is expected that improvement of their Q factors and Q/V, which leads to a reduction of the threshold carrier density required for lasing and sustained lasing over long durations,<sup>[38]</sup> would contribute to the development of electrically pumped semiconductor lasers in future. It is predicted that a  $\text{CH}_3\text{NH}_3\text{PbI}_3$  WGM cavity with absorption of  $5.8 \times 10^3 \text{ cm}^{-1}$  at 780 nm would have a Q factor limit of  $\approx 7 \times 10^4$ .<sup>[33]</sup> However, the Q factors of the resonators are extremely sensitive to surface inhomogeneities because of scattering losses.<sup>[39]</sup> In the absence of contaminants, the Q factor of a WGM cavity may reach the limit defined by the material losses because the scattering losses would be suppressed. Compared to crystalline resonators made through the lithography technique, which currently provide the highest Q factors, a naturally formed perovskite nanocavity is apparently more advantageous for its perfectly grown surface, shape and freedom from complicated machining and photolithographic processes. Consequently, the fabrication of a perovskite NPL WGM cavity without unwanted roughness and impurities that can seriously degrade their performance is of significant importance for laser applications.

Here, we show the growth of an atomically smooth equilateral triangular  $\text{PbI}_2$  NPLs template on an ultrasmooth mica substrate using the vapor phase deposition method. Then, the template is converted into atomically smooth perovskite NPLs. In contrast to the microscopic measurement in ref. [1], which showed fluctuations greater than 20 nm on the perovskite NPL surfaces also based on the vapor phase deposition method, we realized average surface roughnesses of perovskite NPLs of less than 2 nm. By using a  $\text{CH}_3\text{NH}_3\text{PbI}_3$  perovskite NPL with a side length of  $27 \mu\text{m}$  and thickness of 80 nm, we realized room-temperature nearly single-mode lasing in these NPLs with a Q

up to 2600. To the best of our knowledge, this work presents the highest lasing Q factor among all  $\text{CH}_3\text{NH}_3\text{PbI}_3$  NPL devices (the record Q in the literature was 1210 in ref. [36]), and it is also much higher than the Q factor of a  $\text{CH}(\text{NH}_2)_2\text{PbI}_3$  NPL laser cavity with a Q of 1700.<sup>[6]</sup> Moreover, the mode volume of the  $\text{CH}_3\text{NH}_3\text{PbI}_3$  NPL in this work is much smaller than that of the  $\text{CH}_3\text{NH}_3\text{PbI}_3$  NPL with the same geometry reported in ref. [1], yielding a significant improvement in the value of Q/V. Our work contributes to the development of high performance semiconductor lasers.

## 2. Results and Discussion

The  $\text{CH}_3\text{NH}_3\text{PbI}_3$  perovskite triangular NPLs were grown on muscovite mica substrates using a two-step vapor phase deposition method (see the Experimental Section),<sup>[1]</sup> of which the first step is to make the  $\text{PbI}_2$  NPLs template, and the second is to convert the  $\text{PbI}_2$  NPLs into  $\text{CH}_3\text{NH}_3\text{PbI}_3$  NPLs, as shown in Figure S1 (Supporting Information). The  $\text{PbI}_2$  template obtained in the first step determines the morphologies of the following obtained  $\text{CH}_3\text{NH}_3\text{PbI}_3$  NPLs. Our previous work concluded that during the first step deposition, the sizes of the  $\text{PbI}_2$  NPLs can be well-controlled by the distance between the mica substrate and  $\text{PbI}_2$  powder as well as the growth temperature.<sup>[40]</sup> The optical images indicate that the deposited  $\text{PbI}_2$  NPLs show diverse bright colors, and the atomic force microscopy (AFM) analysis of a typical  $\text{PbI}_2$  NPL reveals that its surface is perfectly flat at the optical level with an RMS value below 1 nm (Figure S2, Supporting Information).

In this work, we reduce the surface roughnesses of  $\text{CH}_3\text{NH}_3\text{PbI}_3$  NPLs by optimizing the conditions of the second step conversion process, which includes the tube temperature and the flow velocity of the Ar gas. Detailed comparisons of the  $\text{CH}_3\text{NH}_3\text{PbI}_3$  NPLs obtained under various conditions can be found in Figures S3–S5 (Supporting Information). The successful growth of atomically smooth  $\text{CH}_3\text{NH}_3\text{PbI}_3$  NPLs was realized when the substrate with the  $\text{PbI}_2$  template was attached to the top wall of the tube at a distance of 5 cm downstream from the  $\text{CH}_3\text{NH}_3\text{I}$  powder, the tube temperature was  $20^\circ\text{C}$ , the reaction time was 200 min, and the flow velocity of Ar gas was 34 sccm. Figure 1a is a typical optical image of  $\text{CH}_3\text{NH}_3\text{PbI}_3$  NPLs grown on the mica substrate, which feature well-defined triangular or hexagonal shapes, nanoscale thicknesses (50–150 nm) and microscale edge lengths (20  $\mu\text{m}$  to 70  $\mu\text{m}$ ). The perovskite NPLs show a strong dependence of color on their thicknesses.<sup>[1]</sup> Since the refractive indices of the  $\text{CH}_3\text{NH}_3\text{PbI}_3$  NPLs differ from those of the  $\text{PbI}_2$  NPLs and the thicknesses also vary after the insertion of a methylammonium group in the center of the eight octahedrons, the colors of the  $\text{PbI}_2$  NPLs are changed after conversion into  $\text{CH}_3\text{NH}_3\text{PbI}_3$  NPLs. Figure 1b shows the X-ray diffraction (XRD) patterns of as-grown  $\text{CH}_3\text{NH}_3\text{PbI}_3$  and  $\text{PbI}_2$  NPLs on the mica substrate before and after conversion in the  $\theta$ – $\theta$  geometry. It is clear that, after conversion, the peaks corresponding to 001, 002, 003, 004 of the 2-H lead iodide crystals disappear and several new peaks, which are 110, 220, 310 of tetragonal-phase lead iodide perovskites, are observed, which is in good agreement with the literature.<sup>[41,42]</sup> The disappearance of the  $\text{PbI}_2$  peaks confirmed

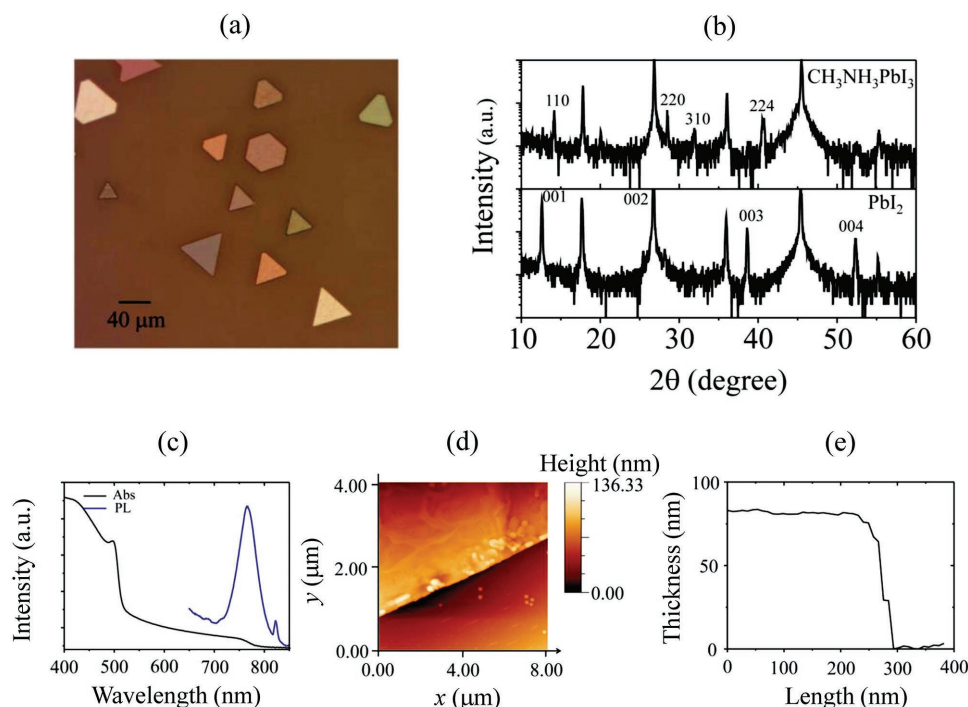


**Figure 1.** a) Optical image of  $\text{CH}_3\text{NH}_3\text{PbI}_3$  NPLs grown on a mica substrate. b) XRD patterns of  $\text{CH}_3\text{NH}_3\text{PbI}_3$  and  $\text{PbI}_2$  NPLs. c) Absorption and photoluminescence spectra taken from a large number of NPLs. d) AFM image of a typical triangular  $\text{CH}_3\text{NH}_3\text{PbI}_3$  NPL edge. e) Cross section of a typical  $\text{CH}_3\text{NH}_3\text{PbI}_3$  NPL edge.

the completed conversion from  $\text{PbI}_2$  to  $\text{CH}_3\text{NH}_3\text{PbI}_3$ .<sup>[42]</sup> Note that the XRD measurements were directly carried out in the  $\text{CH}_3\text{NH}_3\text{PbI}_3$  NPLs on the mica substrate of which the XRD peaks locate at  $17.80^\circ$ ,  $26.86^\circ$ ,  $36.01^\circ$ ,  $45.52^\circ$ , and  $55.21^\circ$  (see Figure S6, Supporting Information). Since the NPLs are thin and sparse distributed on the substrate, the signal-to-noise ratio of the measurement is slightly lower than that of powder X-ray diffraction (PXRD).<sup>[34]</sup> Nevertheless, the direct XRD measurement is closer to the real situation than the PXRD measurement. The absorption (Abs) and photoluminescence (PL) spectra were measured with light illuminating a large number of  $\text{CH}_3\text{NH}_3\text{PbI}_3$  NPLs on the mica substrate at room temperature, and the results are shown in Figure 1c. As can be seen,  $\text{CH}_3\text{NH}_3\text{PbI}_3$  NPLs have a broad optical absorption at wavelengths shorter than 800 nm, which is a good indication of its excellent light harvesting for applications in optoelectronic devices.<sup>[43]</sup> The absorption spectrum displays a maximum at 495 nm, which can be attributed to the transition from the lower valence band to the conduction band minimum.<sup>[44]</sup> Here, the absorption spectra of the  $\text{PbI}_2$  is also given in Figure S7 (Supporting Information) as background. The PL spectrum of  $\text{CH}_3\text{NH}_3\text{PbI}_3$  NPLs presents a Gaussian-shape peak at 765 nm, which is also in good agreement with previous reports.<sup>[44,45]</sup> It is noted that a secondary peak due to defect induced emissions is also observed at 822 nm in the PL spectrum of  $\text{CH}_3\text{NH}_3\text{PbI}_3$  NPLs.<sup>[46]</sup> We also performed an AFM analysis on a single  $\text{CH}_3\text{NH}_3\text{PbI}_3$  NPL. It is clear from Figure 1d that the  $\text{CH}_3\text{NH}_3\text{PbI}_3$  NPL has a regular and unwrinkled facet in this micrometer scale, which is essential for the WGM resonators. Figure 1e shows that the thickness of the  $\text{CH}_3\text{NH}_3\text{PbI}_3$  NPL is

$\approx 80$  nm and the surfaces of both the  $\text{CH}_3\text{NH}_3\text{PbI}_3$  NPL and mica substrate are perfectly flat as well. The average surface roughness of the  $\text{CH}_3\text{NH}_3\text{PbI}_3$  NPL and mica substrate obtained by AFM measurements (Figure S8, Supporting Information) were 1.72 and 2.80 nm, respectively, indicating that both surfaces are atomically smooth. In summary, upon optimization of the deposition processes, the resultant  $\text{CH}_3\text{NH}_3\text{PbI}_3$  NPLs display atomically smooth surfaces and unwrinkled facets, making it possible to achieve the WGM mode lasing with a high Q factor.

Individual perovskite NPLs were optically pumped at room temperature by a femtosecond-pulsed laser through a home-built fluorescence microscope as shown schematically in Figure 2a. The details of the experimental setup are given in the Experimental Section and Figure S9 (Supporting Information). As shorter wavelength would give higher absorption cross section, to yield a lower threshold pump density,<sup>[44,47]</sup> the third harmonic femtosecond lasing at 343 nm is chosen to excite the  $\text{CH}_3\text{NH}_3\text{PbI}_3$  NPLs instead of the second harmonic one at 515 nm. The pulsed laser beam, with the beam waist adjusted to be larger than the length of each NPL, was used as a nearly uniform pump source. Figure 2b shows a 2D pseudocolor plot of the emission spectra as a function of pump density ( $P$ ) for an equilateral triangular  $\text{CH}_3\text{NH}_3\text{PbI}_3$  NPL with a side length of 27  $\mu\text{m}$ . At low pump density  $P < 18.7 \mu\text{J cm}^{-2}$ , each emission spectrum shows a broad peak centered at 759.3 nm with a full-width at half-maximum (FWHM) of  $\Delta\lambda = 43$  nm, which corresponds to spontaneous emission (SPE). At  $P_{\text{Th}} = 18.7 \mu\text{J cm}^{-2}$ , a sharp peak at 779.12 nm appears and grows rapidly with increasing  $P$ , and the intensity of the broad SPE peak (non-lasing) remains almost constant. The inset in Figure 2b shows

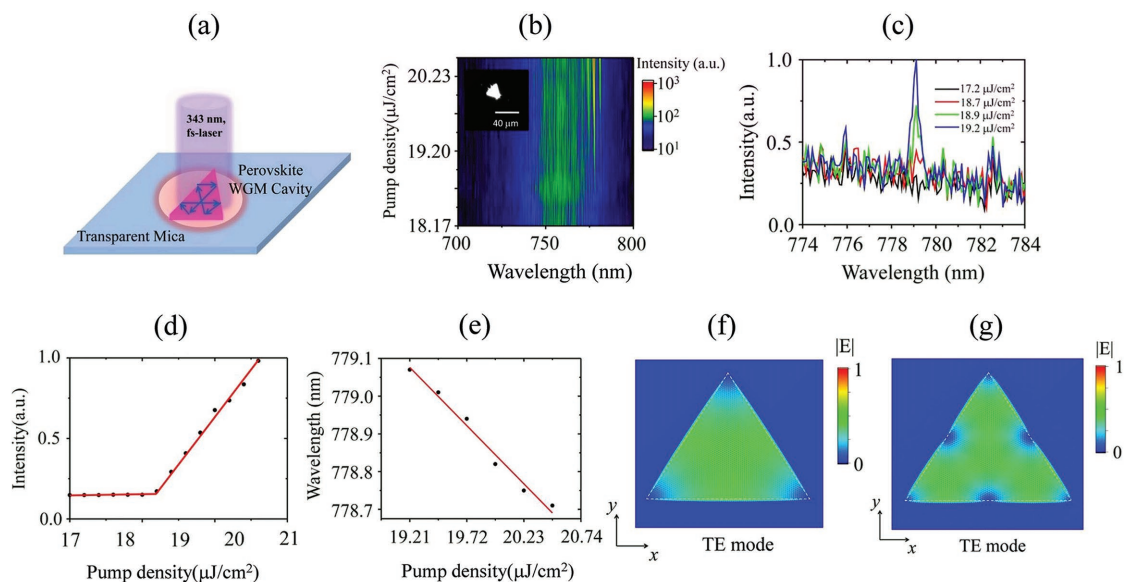


**Figure 2.** a) Schematic of an NPL on mica substrate pumped by 343 nm laser excitation ( $\approx 290$  fs, 6 kHz). b) 2D pseudocolor plot of an equilateral triangular  $\text{CH}_3\text{NH}_3\text{PbI}_3$  NPL emission under different pump densities ( $P$ ) showing broad spontaneous emission spectra below the threshold of  $\approx 18.7 \mu\text{J cm}^{-2}$  and a sharp lasing peak above the threshold. Inset: optical image of a single NPL with a side length of  $27 \mu\text{m}$  pumped above  $P_{\text{Th}}$ . c) NPL emission spectra around the lasing threshold. The FWHM of the lasing spectrum at  $19.2 \mu\text{J cm}^{-2}$  is  $0.3 \text{ nm}$ , corresponding to a Q factor of  $\approx 2600$ . d) Integrated emission intensity as a function of  $P$  showing the lasing threshold of  $18.7 \mu\text{J cm}^{-2}$ . e) The central wavelength as a function of  $P$  shows a small blue shift with increasing pump density. f,g) Electric field distributions of the fundamental WGM mode ( $l = 0$ ) and the higher order WGM mode ( $l = 1$ ) of an equilateral triangular  $\text{CH}_3\text{NH}_3\text{PbI}_3$  NPL.

the emission image of the NPL above  $P_{\text{Th}}$ . Representative emission spectra near the lasing threshold are shown in Figure 2c. The FWHM at  $P = 19.2 \mu\text{J cm}^{-2}$ , at which pump density the lasing peak dominates, is  $0.3 \text{ nm}$  (Figure S10a in the Supporting Information for Lorentz fit). Here, it is noted that the FWHM measurement reaches the spectral resolution limit of our instrument, and the actual FWHM of the lasing peaks of the prepared  $\text{CH}_3\text{NH}_3\text{PbI}_3$  NPLs may be even narrower. Figure 2d shows the light-in light-out (L-L) data as a function of  $P$ , which gives a lasing threshold of  $P_{\text{Th}} = 18.7 \mu\text{J cm}^{-2}$ . The FWHM is a constant value below  $P_{\text{Th}}$  and drops suddenly by more than two orders of magnitude at  $P_{\text{Th}}$  (Figure S10b, Supporting Information). Figure S10c (Supporting Information) presents L-L data as a function of  $P$  with a large pump density range including the saturation regime in log-log scale. It is seen that at the low excitation regime below the lasing threshold, the PL emission increases linearly with the increase of the pump density. Above the lasing threshold, the emission first increases, and then gets saturation at a pump density of  $20.74 \mu\text{J cm}^{-2}$  and gradually falls down. Experimentally, the Q-factor of a cavity is expressed as  $Q = \lambda/\lambda_{\text{FWHM}}$ , where  $\lambda$  is the center wavelength and  $\lambda_{\text{FWHM}}$  is the FWHM of its spectrum. The lasing spectra in Figure 2c at  $P = 19.2 \mu\text{J cm}^{-2}$  gives a quality factor  $Q = 2600$ , which far exceeds the performances of all afore-demonstrated  $\text{CH}_3\text{NH}_3\text{PbI}_3$  NPL based lasers and is also higher than the Q factor of a  $\text{CH}(\text{NH}_2)_2\text{PbI}_3$  NPL laser.<sup>[1,2,6,29,36]</sup> Such a high Q factor of the induced lasing action results from the perfectly flat surfaces and unwrinkled facets of the prepared  $\text{CH}_3\text{NH}_3\text{PbI}_3$  NPLs, which provide high quality mirrors with high reflectivity for the optical cavity, thereby reducing dissipation from the surface. It is worthwhile to mention that all the spectrum

measurements were carried out by a room temperature CCD, of which the noise is higher than that detected by a liquid-N<sub>2</sub>-cooled one.<sup>[34]</sup> In fact, the high output intensity of the laser significantly minimizes the influence of the noise at room temperature, yielding high signal to noise ratio larger than 1. The above result provides excellent evidence that the WGM resonance in a naturally formed high-quality triangular  $\text{CH}_3\text{NH}_3\text{PbI}_3$  NPL can provide strong optical confinement and induce lasing action with longer excitation pulse duration.

We note a small blueshift of the central wavelength, as shown in Figure 2e, and broadening of the FWHM with increasing pump power. The blueshift with increasing carrier density has also been observed previously in  $\text{CH}_3\text{NH}_3\text{PbI}_3$  nanowire (NW) lasers.<sup>[34]</sup> It has been assumed to originate from the thermally induced bandgap/refractive index change, band filling, optical density fluctuations, and electron/hole many-body interactions. It is also worth mentioning that our demonstration of a 2600 Q factor carried out for a  $\text{CH}_3\text{NH}_3\text{PbI}_3$  NPL with a side length of  $27 \mu\text{m}$  and thickness of  $80 \text{ nm}$  has a much smaller mode volume than that reported in ref. [1], which used a triangular  $\text{CH}_3\text{NH}_3\text{PbI}_3$  NPL with a side length of  $32 \mu\text{m}$  and thickness of  $150 \text{ nm}$  to realize a Q factor of 650. A remarkable improvement of Q/V is obtained for the equilateral  $\text{CH}_3\text{NH}_3\text{PbI}_3$  NPL cavity, which is beneficial for lowering the lasing threshold if strong coupling conditions are satisfied.<sup>[21]</sup> The cavity with a smaller thickness shows a shorter PL lifetime or faster radiative rate.<sup>[48]</sup>

As can be seen in Figure 2c, the  $27 \mu\text{m}$   $\text{CH}_3\text{NH}_3\text{PbI}_3$  NPL shows three WGM cavity modes, among which the central mode located at  $779.08 \text{ nm}$  experiences the largest net gain and whose intensity grows faster than those of the other two

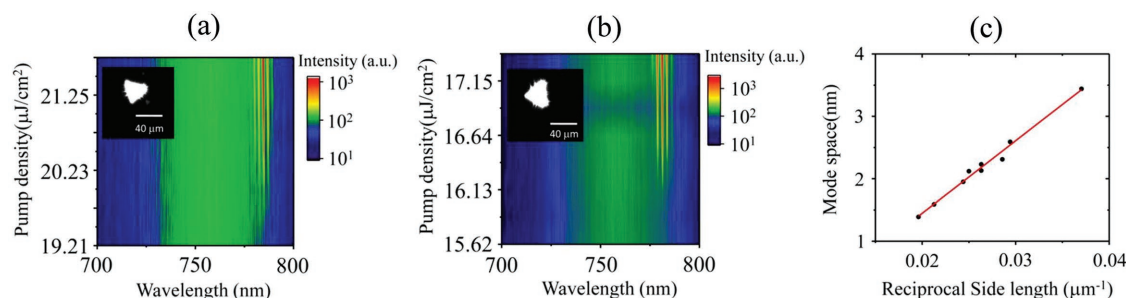


**Figure 3.** 2D pseudocolor plots of pump-density-dependent emission spectra of equilateral triangular  $\text{CH}_3\text{NH}_3\text{PbI}_3$  NPLs with side lengths of a) 40  $\mu\text{m}$  and b) 46  $\mu\text{m}$ . c) Mode spacing of the lasing peaks as a function of the reciprocal of the NPL side length (solid circles). The experimental data are well-fitted by a linear function.

modes at 775.94 and 782.56 nm. To explain this, the waveguide modes in the equilateral triangular NPLs were analyzed using a finite-element method (see Simulation Methods in the Supporting Information). The waveguide modes are strictly transverse electric modes (abbreviated as TE modes) with the electric field in the plane of the triangle. For the transverse magnetic modes (TM modes), with the magnetic field in the plane of the triangle, the effective refractive index of the semiconductor is lower than 2.0, and the total internal reflection condition cannot be satisfied. The resonant mode wavelength inside an equilateral triangle microresonator can be expressed as  $\lambda_{l,m} = 3na/\sqrt{l^2 + 3(m+1)^2}$  when the phase shifts for waves at the edges of the triangular sides are neglected.<sup>[49]</sup> Here,  $l$  and  $m$  represent the mode indices of the longitudinal mode and transverse mode, respectively, and their sum must be an even integer;  $a$  denotes the side length of the triangle; and  $n$  denotes the effective wavelength of the TE mode propagating within the plane of the triangular NPL. Figure 2f shows the fundamental mode with  $l = 0$ , which means the segments of the light circulating path are always parallel to one of the sides, as shown in Figure 2a. It is seen that for TE cases, the optical fields are reflected between the triangle facets to construct WGM waveguides that are well-confined inside the cavities. Because the side length of the NPL is much larger than the effective wavelength of the WGM mode, the nodes produced by the transverse mode resonance cannot be witnessed in the length scale shown in Figure 2f. In such a case, the Q factor of the cavity resonance is pretty high because the total internal reflections are produced at the NPL facets. Thus, the central peak at 779.12 nm corresponds to the fundamental WGM mode of the lasing action for the prepared perovskite NPL. When the longitudinal mode that has each segment of the light circulating path perpendicular to one of the three sides participates in the WGM resonances, the Q factor of the cavity resonance degrades significantly because the reflectance at perpendicular incidence with respect to the side of the triangle is much lower than that of the total internal reflection case. Figure 2g displays the mode distribution for  $l = 1$ , with one node along each side of the triangle. It is noted that with increasing index of the transverse mode, the WGM mode shifts to a different wavelength, and, simultaneously, the longitudinal mode changes from odd to even or vice versa because the sum of  $m$  and  $l$  must be an even integer. Thus, the two lower peaks at 775.94 nm and 782.56 nm in Figure 2c correspond to high order WGM resonances with  $l = 1$  that have

a mode distribution as shown in Figure 2f. At a fixed  $m$ , the increase of  $l$  induces other high order WGM resonances, but they suffer high losses, and thus poor Q factors, due to poor reflection at perpendicular incidence with respect to the side of the triangle. Here, the wavelength shift between different WGM cavity modes in Figure 2c, denoted as the mode space ( $\Delta\lambda$ ), arises from the changes of the mode indices of both the transverse mode and longitudinal mode. However,  $m$  plays a major role in shifting the wavelength peak of the WGM resonances because in the expression for  $\lambda_{l,m}$ ,  $m$ , which is produced due to light circulation parallel to the sides, is much greater than  $l$ , with the light path perpendicular to the sides. Figure 2c shows that the predominance of the strongest mode at 779.12 nm results in nearly single-frequency operation. Moreover, by adjusting the resonant wavelength toward the emission peaks (e.g., by decreasing the side length of  $\text{CH}_3\text{NH}_3\text{PbI}_3$  NPLs), the threshold pump density may be further reduced.

In the following, the influences of the size of the  $\text{CH}_3\text{NH}_3\text{PbI}_3$  NPL on the mode confinement and the lasing threshold have been investigated at room temperature. Figure 3a,b shows the typical lasing spectra of equilateral triangular  $\text{CH}_3\text{NH}_3\text{PbI}_3$  NPLs with side lengths of 40  $\mu\text{m}$  and 46  $\mu\text{m}$ , respectively. Similar to the phenomenon observed for the 27  $\mu\text{m}$   $\text{CH}_3\text{NH}_3\text{PbI}_3$  NPL, at low pump density illumination, the emission spectra are broad; after the pumping power exceeds the threshold, sharp peaks appear. As the edge length of the  $\text{CH}_3\text{NH}_3\text{PbI}_3$  NPLs increases from 40 to 46  $\mu\text{m}$ , a shift of the sharp peaks can be seen. The corresponding L-L plots can be found in Figure S11 (Supporting Information). It is found that the lasing thresholds for the single crystal  $\text{CH}_3\text{NH}_3\text{PbI}_3$  NPLs vary from NPL to NPL: from 16.4 to 20.2  $\mu\text{J cm}^{-2}$ , without a clear dependence on the NPL side length (see Figure S11, Supporting Information) which might be ascribed to the variation of surface roughnesses of different NPLs. It has been reported that the Q factor of  $\text{CH}_3\text{NH}_3\text{PbI}_3$  NPLs increases linearly with the side length.<sup>[1]</sup> We expect that higher Q factors can be achieved with NPLs with longer side lengths. However, limited by the resolution of our spectrometer, we cannot demonstrate it in this paper. We further investigate the lasing mode as a function of the NPLs side lengths. With the increase of NPLs side lengths,  $a$ , from 27 to 51  $\mu\text{m}$ , the spacing between two adjacent mode decreases from 3.44 to 1.39 nm, which is well-fitted by a linear function (Figure 3c). This observation is in good agreement with the relationship for mode spacing

$\Delta\lambda = \lambda^2/na$ ,<sup>[50]</sup> which can be easily derived from the expression for  $\lambda_{l,m}$ .

### 3. Conclusion

In conclusion, we have demonstrated the growth of atomically smooth  $\text{CH}_3\text{NH}_3\text{PbI}_3$  NPLs by growing atomically smooth triangular  $\text{PbI}_2$  NPL template on an ultrasmooth mica substrate and then converting it into perovskite. By using an atomically smooth equilateral triangular  $\text{CH}_3\text{NH}_3\text{PbI}_3$  NPL with a side length of 27  $\mu\text{m}$  and thickness of 80 nm, we realized room-temperature WGM lasing with a threshold down to 18.7  $\mu\text{J cm}^{-2}$  and a Q factor up to 2600. The exceptional lasing performance of lead halide perovskite equilateral triangular NPLs can be attributed to the improved (reduced) surface roughness and unwrinkled facets. Notably, the realized Q factor in this work is considerably higher than all previously reported results among the  $\text{CH}_3\text{NH}_3\text{PbI}_3$  NPL lasers, suggesting that exceptionally low surface trap densities and the cavity scattering losses are well overcompensated by high optical gain of the material.<sup>[33]</sup> In combination with the remarkably high Q factor, the present  $\text{CH}_3\text{NH}_3\text{PbI}_3$  NPL yields significantly stronger coupling between the gain medium and the cavity field than do the thicker ones reported in literature. In view of the ease of growth, large quality factor, small mode volume, and efficient gain–cavity coupling, the equilateral triangular  $\text{CH}_3\text{NH}_3\text{PbI}_3$  perovskite NPLs may become ideal cavity of choice for implementation of semiconductor lasers in a wide range of applications.

### 4. Experimental Section

**Synthesis of Perovskite NPLs:**  $\text{PbI}_2$  (99.999%, Alfa) was used as a single source and placed into a quartz tube mounted on a single zone furnace (CY scientific instrument, CY-O1200-1L) at a room temperature of 18 °C. The fresh-cleaved muscovite mica substrate was precleaned with acetone and placed in the downstream region inside the quartz tube. The quartz tube was first evacuated to 0.025 MPa, followed by a 30 sccm flow of high purity Ar premixed with 10%  $\text{H}_2$  gas. The temperature and pressure inside the quartz tube were set and stabilized at 380 °C and 0.12 MPa for  $\text{PbI}_2$ . The synthesis of  $\text{PbI}_2$  was completed within 14 min, and the furnace was allowed to cool naturally to room temperature. Then, pregrown lead halide platelets were thermally intercalated with methylammonium iodide (Xi'an Polymer light technology) in a fresh quartz tube. The platelets were placed in the downstream region, while the methylammonium iodide was placed in the center of the tube. The intercalation was carried out at 120 °C at a pressure of 0.11 MPa with a 34 sccm flow of high purity Ar for 200 min to fully convert the lead halides to perovskites.

**Image and Phase Characterizations:** The optical images of  $\text{CH}_3\text{NH}_3\text{PbI}_3$  nanostructures were obtained on a Nikon LV150 optical microscope. The AFM images were collected on an FM-Nanoview 1000 AFM (FSM Precision). The XRD data were acquired on a DX-2700 diffractometer (Dandong Yaoyuan).

**Optical Spectrum Characterization:** Steady-state PL spectra were measured at room temperature using an Edinburgh FLS980 Spectrometer. An XBO450/OFR ozone-free xenon arc lamp was used as the excitation source. The absorption spectra of perovskite NPLs were obtained at room temperature using a Shimadzu UV-2600 UV-VIS Spectrometer. We carried out optically pumped lasing measurements on a home-built microscope setup. The 343 nm excitation pulses were

generated by frequency tripling the 1028 nm output (with a BBO crystal) from a Light Conversion Carbide Femtosecond laser (290 fs, 6 kHz, 1028 nm). The pumping source was focused onto samples via an uncoated convex lens (Focal length: 20 cm, Transmittance: 93.4%). To ensure uniform energy injection, the laser spot diameter was focused to  $\approx 88 \mu\text{m}$  which was measured by imaging the laser spot onto a camera (see Figure S12, Supporting Information). The transmitted emission was collected through a 20 $\times$  objective (Olympus, Numerical Aperture: 0.4). Half of the emission signals were imaged on a camera (Hamamatsu, C11440-36U). The other half of the emission signals from a single NPL were collected into an optical fiber and analyzed using an ideaoptics PG2000Pro spectrometer with a wavelength resolution (FWHM) of 0.3 nm.

### Supporting Information

Supporting Information is available from the Wiley Online Library or from the author.

### Acknowledgements

This research was funded by the National Natural Science Foundation of China (61605136, 61775156, 61475109, and U1710115), Young Sanjin Scholars Program, and Open Project from the State Key Laboratory of Quantum Optics and Quantum Optics Devices at Shanxi Province (KF201803). S.L. also acknowledges support from the National Key Research and Development Program of China (2017YFA0204800 and 2016YFA0202403), the National Natural Science Foundation of China (61674098), the 111 Project (B14041), and the Changjiang Scholar and Innovative Research Team (IRT\_14R33).

### Conflict of Interest

The authors declare no conflict of interest.

### Keywords

atomically smooth, lasers, low-threshold, nanoplatelet perovskites

Received: August 10, 2018

Revised: September 26, 2018

Published online:

- [1] Q. Zhang, S. T. Ha, X. Liu, T. C. Sum, Q. Xiong, *Nano Lett.* **2014**, 14, 5995.
- [2] Q. Liao, K. Hu, H. Zhang, X. Wang, J. Yao, H. Fu, *Adv. Mater.* **2015**, 27, 3405.
- [3] W. S. Yang, B. W. Park, E. H. Jung, N. J. Jeon, Y. C. Kim, D. U. Lee, S. S. Shin, J. Seo, E. K. Kim, J. H. Noh, S. I. Seok, *Science* **2017**, 356, eaah6345.
- [4] Z. Wang, Q. Lin, F. P. Chmie, N. Sakai, L. M. Herzand, H. J. Snaith, *Nat. Energy* **2017**, 2, 17135.
- [5] N. Arora, M. I. Dar, A. Hinderhofer, N. Pellet, F. Schreiber, S. M. Zakeeruddin, M. Grätzel, *Science* **2017**, 358, 768.
- [6] Y. Fu, T. Wu, J. Wang, J. Zhai, M. J. Shearer, Y. Zhao, R. J. Hamers, E. Kan, K. Deng, X.-Y. Zhu, S. Jin, *Nano Lett.* **2017**, 17, 4405.
- [7] M. A. Green, A. Ho-Baillie, H. J. Snaith, *Nat. Photonics* **2014**, 8, 506.
- [8] B. R. Sutherland, E. H. Sargent, *Nat. Photonics* **2016**, 10, 295.
- [9] Y. Zhang, Y. Liu, Y. Li, Z. Yang, S. Liu, *J. Mater. Chem. C* **2016**, 4, 9172.

- [10] Y. Zhang, Y. Liu, Z. Yang, S. Liu, *J. Energy Chem.* **2018**, 27, 722.
- [11] X. J. Liu, Y. C. Liu, F. Gao, Z. Yang, S. Liu, *Appl. Phys. Lett.* **2016**, 108, 181604.
- [12] Y. C. Liu, Z. Yang, D. Cui, X. D. Ren, J. K. Sun, X. J. Liu, J. R. Zhang, Q. B. Wei, H. B. Fan, F. Y. Yu, X. Zhang, C. M. Zhao, S. Liu, *Adv. Mater.* **2015**, 27, 5176.
- [13] Y. C. Liu, Y. X. Zhang, Z. Yang, D. Yang, X. D. Ren, L. Q. Pang, S. Liu, *Adv. Mater.* **2016**, 28, 9204.
- [14] Y. C. Liu, J. K. Sun, Z. Yang, D. Yang, X. D. Ren, H. Xu, Z. P. Yang, S. Z. Liu, *Adv. Opt. Mater.* **2016**, 4, 1829.
- [15] Y. C. Liu, X. D. Ren, J. Zhang, Z. Yang, D. Yang, F. Y. Yu, J. K. Sun, C. M. Zhao, Z. Yao, B. Wang, Q. B. Wei, F. W. Xiao, H. B. Fan, H. Deng, L. P. Deng, S. Liu, *Sci. China Chem.* **2017**, 60, 1367.
- [16] Y. C. Liu, Z. Yang, S. Liu, *Adv. Sci.* **2018**, 5, 1700471.
- [17] M. T. Hill, M. C. Gather, *Nat. Photonics* **2014**, 8, 908.
- [18] C. Grivas, C. Li, P. Andreakou, P. Wang, M. Ding, G. Brambilla, L. Manna, P. Lagoudakis, *Nat. Commun.* **2013**, 4, 2376.
- [19] J. Norman, M. J. Kennedy, J. Selvidge, Q. Li, Y. Wan, A. Y. Liu, P. G. Callahan, M. P. Echlin, T. M. Pollock, K. M. Lau, A. C. Gossard, J. E. Bowers, *Opt. Express* **2017**, 25, 3927.
- [20] T. Nobis, E. M. Kaidashev, A. Rahm, M. Lorenz, M. Grundmann, *Phys. Rev. Lett.* **2004**, 93, 103903.
- [21] S. M. Spillane, T. J. Kippenberg, K. J. Vahala, *Nature* **2002**, 415, 621.
- [22] A. Chiasera, Y. Dumeige, P. Féron, M. Ferrari, Y. Jestin, G. N. Conti, S. Pelli, S. Soria, G. C. Righini, *Laser Photonics Rev.* **2010**, 4, 457.
- [23] L. He, S. K. Özdemir, L. Yang, M. T. Hill, M. C. Gather, *Laser Photon. Rev.* **2013**, 7, 60.
- [24] S. L. McCall, A. F. J. Levi, R. E. Slusher, S. J. Pearton, R. A. Logan, *Appl. Phys. Lett.* **1992**, 60, 289.
- [25] D. J. Gargas, M. C. Moore, A. Ni, S. Chang, Z. Zhang, S. Chuang, P. Yang, *ACS Nano* **2010**, 4, 3270.
- [26] R. Chen, B. Ling, X. W. Sun, H. D. Sun, *Adv. Mater.* **2011**, 23, 2199.
- [27] R. Chen, T. D. Tran, K. W. Ng, W. S. Ko, L. C. Chuang, F. G. Sedgwick, C. Chang-Hasnain, *Nat. Photonics* **2011**, 5, 170.
- [28] K. Okazaki, T. Shimogaki, K. Fusazaki, M. Higashihata, D. Nakamura, N. Koshizaki, T. Okada, *Appl. Phys. Lett.* **2012**, 101, 211105.
- [29] P. Perumal, C. Wang, K. M. Boopathi, G. Haider, W.-C. Liao, Y.-F. Chen, *ACS Photonics* **2017**, 4, 146.
- [30] B. Tang, H. Dong, L. Sun, W. Zheng, Q. Wang, F. Sun, X. Jiang, A. Pan, L. Zhang, *ACS Nano* **2017**, 11, 10681.
- [31] X. Tang, Z. Hu, W. Yuan, W. Hu, H. Shao, D. Han, J. Zheng, J. Hao, Z. Zang, J. Du, Y. Leng, L. Fang, *Adv. Opt. Mater.* **2017**, 5, 1600788.
- [32] Q. Zhang, R. Su, X. Liu, J. Xing, T. C. Sum, Q. Xiong, *Adv. Funct. Mater.* **2016**, 26, 6238.
- [33] G. Xing, N. Mathews, S. S. Lim, N. Yantara, X. Liu, D. Sabba, M. Grätzel, S. Mhaisalkar, T. C. Sum, *Nat. Mater.* **2014**, 13, 476.
- [34] H. Zhu, Y. Fu, F. Meng, X. Wu, Z. Gong, Q. Ding, M. V. Gustafsson, M. T. Trinh, S. Jin, X.-Y. Zhu, *Nat. Mater.* **2015**, 14, 636.
- [35] M. Saliba, S. M. Wood, J. B. Patel, P. K. Nayak, J. Huang, J. A. Alexander-Webber, B. Wenger, S. D. Stranks, M. T. Hörantner, J. T. Wang, R. J. Nicholas, L. M. Herz, M. B. Johnston, S. M. Morris, H. J. Snaith, M. K. Riede, *Adv. Mater.* **2016**, 28, 923.
- [36] X. Liu, L. Niu, C. Wu, C. Cong, H. Wang, Q. Zeng, H. He, Q. Fu, T. Yu, C. Jin, Z. Liu, T. C. Sum, *Adv. Sci.* **2016**, 3, 1600137.
- [37] K. Wang, W. Sun, J. Li, Z. Gu, S. Xiao, Q. Song, *ACS Photonics* **2016**, 3, 1125.
- [38] M. Cadelano, V. Sarritzu, N. Sestu, D. Marongiu, F. Chen, R. Piras, R. Corpino, C. M. Carbonaro, F. Quochi, M. Saba, A. Mura, G. Bongiovanni, *Adv. Opt. Mater.* **2015**, 3, 1557.
- [39] M. L. Gorodetsky, A. A. Savchenkov, V. S. Ilchenko, *Opt. Lett.* **1996**, 21, 453.
- [40] W. Kong, G. Li, Q. Liang, X. Ji, G. Li, T. Ji, T. Che, Y. Hao, Y. Cui, *Phys. E* **2018**, 97, 130.
- [41] S. Sun, T. Salim, N. Mathews, M. Duchamp, C. Boothroyd, G. Xing, T. C. Sum, Y. M. Lam, *Energy Environ. Sci.* **2014**, 7, 399.
- [42] S. T. Ha, X. Liu, Q. Zhang, D. Giovanni, T. C. Sum, Q. Xiong, *Adv. Opt. Mater.* **2014**, 2, 838.
- [43] Q. Dong, Y. Fang, Y. Shao, P. Mulligan, J. Qiu, L. Cao, J. Huang, *Science* **2015**, 347, 967.
- [44] A. Yang, M. Bai, X. Bao, J. Wang, W. Zhang, *J. Nanomed. Nanotechnol.* **2016**, 7, 5.
- [45] Z. Xie, S. Liu, L. Qin, S. Pang, W. Wang, Y. Yan, L. Yao, Z. Chen, S. Wang, H. Du, M. Yu, G. G. Qin, *Opt. Express* **2014**, 5, 29.
- [46] A. Dey, P. Rathod, D. Kabra, *Adv. Opt. Mater.* **2018**, 6, 1800109.
- [47] Z. Li, D. Psaltis, *Microfluid. Nanofluid.* **2008**, 4, 145.
- [48] V. A. Hintermayr, A. F. Richter, F. Ehrat, M. Döblinger, W. Vanderlinden, J. A. Sichert, Y. Tong, L. Polavarapu, J. Feldmann, A. S. Urban, *Adv. Mater.* **2016**, 28, 9478.
- [49] Y.-Z. Huang, W.-H. Guo, L.-J. Yu, H.-B. Lei, *IEEE J. Quantum Electron.* **2001**, 37, 1259.
- [50] H. C. Chang, G. Kioseoglou, E. H. Lee, J. Haetty, M. H. Na, Y. Xuan, H. Luo, A. Petrou, A. N. Cartwright, *Phys. Rev. A* **2000**, 6, 013826.